Atmos. Chem. Phys. Discuss., 11, 26897–26941, 2011
www.atmos-chem-phys-discuss.net/11/26897/2011/
doi:10.5194/acpd-11-26897-2011

Atmospheric Chemistry and Physics Discussions

Five blind men and an elephant: can NASA Aura measurements quantify the stratosphere-troposphere exchange of ozone flux?

Q. Tang and M. J. Prather

Department of Earth System Science, University of California, Irvine, California, 92697, USA

Received: 17 September 2011 – Accepted: 27 September 2011
– Published: 29 September 2011

Correspondence to: Q. Tang (tangq@uci.edu)

Published by Copernicus Publications on behalf of the European Geosciences Union.

Abstract

We examine whether the instantaneous ozone (O_3) measurements from the four Aura instruments can quantify the stratosphere-troposphere exchange (STE) flux of O_3, an important term of the tropospheric O_3 budget. Comparing the level 2 (L2) Aura swaths and ozone sondes with the coincident, high-resolution ($1^\circ \times 1^\circ \times 40$-layer$\times 0.5$ h) simulations using the University of California, Irvine chemistry transport model (CTM) for years 2005–2006, it is revealed in many cases that all four Aura datasets have some skill in catching the STE process, while missing many of them. Despite a few cases, the individual retrievals in the upper troposphere and lower stratosphere contain too much noise preventing the quantification and integration of STE flux with Aura L2 data. The CTM is applied as a transfer standard to compare with different Aura observations. The statistics of exact matching CTM-Aura comparisons identify the model's high biases in the lower stratosphere and the inconsistency amongst different instruments, such as from tropics to Northern Hemisphere mid-latitudes in July 2005 at 215 hPa and over tropics at 147 hPa for July 2005 and January 2006.

1 Introduction

Quantifying and understanding the causes of changes in tropospheric ozone burden are important topics for climate research and environmental studies, as ozone is a major greenhouse gas and plays a key role in the tropospheric chemistry. Besides obvious factors such as anthropogenic emissions of ozone precursors (Gauss et al., 2006; Hoor et al., 2009; Myhre et al., 2011; Holmes et al., 2011) and natural emissions of biogenic volatile organic compounds (Atkinson and Arey, 2003; Shao et al., 2009), stratospheric ozone influx has been identified as a major driver of tropospheric ozone changes (e.g., Roelofs and Lelieveld, 1997; Fusco and Logan, 2003; Terao et al., 2008; Hsu and Prather, 2009). There are large uncertainties in the estimates of global annual stratosphere-troposphere exchange (STE) of ozone flux

ACPD
11, 26897–26941, 2011

either derived from observations (450 $Tg(O_3)\,yr^{-1}$ (range, 200–870) (Murphy and Fahey, 1994), 510 $Tg(O_3)\,yr^{-1}$ (450–590) (Gettelman et al., 1997), 550 ± 140 $Tg(O_3)\,yr^{-1}$ (Olsen et al., 2001)) or from model simulations (e.g., Denman et al., 2007, Table 7.9 and references therein). There are also disagreements in terms of the magnitude and phase of the annual cycle as well as the geographical patterns (e.g., Gettelman et al., 1997; Roelofs and Lelieveld, 1997; Olsen et al., 2004; Hsu et al., 2005; Hsu and Prather, 2009). The large uncertainties and differences in the assessments of the STE O_3 budget are partly due to the different diagnostic methods used in these studies and partly due to the great temporal and spatial variances of the STE flux.

The four Earth Observing System (EOS) Aura satellite ozone measurements (the High Resolution Dynamics Limb Sounder (HIRDLS), the Microwave Limb Sounder (MLS), the Ozone Monitoring Instrument (OMI), and the Tropospheric Emission Spectrometer (TES)) plus the coincident ozone sondes flown for calibration/validation of the satellite instruments comprise a somewhat overlapping set of five different ozone measurements. We merge these five with the University of California, Irvine (UCI) chemistry transport model (CTM) simulations with the overall goal of using the model and measurements to derive a better understanding of how the stratospheric source affects the tropospheric ozone abundance. We evaluate if the Aura ozone measurements can resolve processes, such as tropopause folds (TFs) (Danielsen, 1968), relate these events to STE O_3 fluxes; and examine the consistency amongst different Aura datasets, particularly in the upper troposphere and lower stratosphere (UT/LS) region (300–100 hPa). The UT/LS is where the influx of stratospheric O_3 is most evident (Terao et al., 2008) and where O_3 has the largest impact on radiative forcing of climate (Lacis et al., 1990). We draw on the parable of the five blind men and the elephant, where the five Aura measurements are the five "blind men" who are touching the "elephant" (ozone) in different places (i.e., using different remote sensing techniques and observing different parts of the atmosphere (OMI and TES have some overlap)). The UCI CTM is able to see the whole "elephant" and thus provides an intercomparison platform to relate the different Aura ozone measurements.

ACPD
11, 26897–26941, 2011

2 Chemistry transport model

The chemistry transport model (CTM) is forced by the pieced-forecast meteorological fields provided by University of Oslo (Kraabøl et al., 2002; Isaksen et al., 2005) from the European Centre for Medium-Range Weather Forecasts (ECMWF) Integrated Forecast System (IFS). The model is initialized on 1 January 2005 (00:00 UTC) with a restart file from a CTM simulation ending 31 December 2004 at a resolution of T42 (~2.8°× ~2.8°) 40-layer and then run through 31 December 2006 at 1°×1°×40-layer×0.5 h resolution. The 1°×1° meteorological fields are only available for two years (2005–2006). The modeled atmosphere extends from the surface to 2 hPa with ~1 km vertical resolution around the tropopause. Because the interpolation from the T42 grid to the 1°×1° grid introduces errors at the beginning of the 1°×1° simulation, the quantitative analysis here often omits the first few months. The primary model output for this analysis is a 65-min swath along the Aura orbit every half an hour (30 min backward and 35 min forward from the sampling point) so that we can interpolate the overlapped swaths to match the exact time and location of each Aura measurement. The additional 5-min forward swath is designed to cover the MLS observations scanning in the forward limb direction. The swath is wide enough to include the cross-track scan of OMI and the off-track viewing geometry of HIRDLS, which is outside the OMI swath. We also store 65° S–65° N O_3 field every two hours to match sondes.

The UCI CTM simulates the full tropospheric chemistry with the ASAD (A Self-contained Atmospheric chemistry coDe) software package (Carver et al., 1997) and simplified stratospheric O_3 chemistry with Linoz version 2 (Hsu and Prather, 2009). The ASAD package includes the updates for the chemistry solver (Tang and Prather, 2010) and the chemical kinetics and photochemical coefficients (Sander et al., 2006). The tropopause is diagnosed by the abundance of an artificial tracer e90 (Prather et al., 2011; Tang et al., 2011), which has been demonstrated to match the traditional, but more-awkward-for-our-model definitions. The emissions are taken from the European Union Quantifying the Climate Impact of Global and European Transport Systems

ACPD
11, 26897–26941, 2011

(QUANTIFY) project Year-2000 inventory (Hoor et al., 2009). Advection uses the second order moment scheme (Prather, 1986), and the convection scheme follows Tiedtke (1989).

3 Ozone sonde data

In this study, we use the World Ozone and Ultraviolet Radiation Data Centre (WOUDC) ozone sondes in years 2005–2006 from 42 stations (http://www.woudc.org, retrieved on 10 November 2010) for latitudes 65° S–65° N, which covers most folding events found in the model. The modeled ozone profiles generally match sondes (see Tang and Prather, 2010, Fig. 1). The search criteria for identifying TFs follows the algorithm in Tang and Prather (2010): the O_3 abundance exceeds 80 ppb at an altitude greater than 5 km and it decreases by at least 20 ppb within the 3 km above the peak to a minimum value less than 120 ppb.

4 Aura ozone data and method

The EOS Aura satellite was launched on 15 July 2004 with four ozone instruments (HIRDLS, MLS, OMI, and TES) on board (Schoeberl et al., 2006). Aura flies on a sun-synchronous orbit with a 98° inclination and an ascending equator-crossing time of 13:45 local time. The orbit is 705 km above the sea level with a 16-day repeat period and a single orbit takes ~98 min. In this study, we use the level 2 (L2) swath data from all the four instruments. Many studies of the Aura ozone data use L3 data which are averaged over time, often monthly, and over large grid cells, which smears the real meteorological variability.

ACPD
11, 26897–26941, 2011

4.1 HIRDLS

HIRDLS observes the atmosphere in limb direction at 21 infrared channels from 6.12 to 17.76 µm (HIRDLS Team, 2010). After launch, ~80 % blockage of its optical path was diagnosed, which limited the coverage from 65° S to 82° N, missing the Antarctic. With its limited field of view at one azimuth angle, however, HIRDLS can still retrieve ozone profiles (260–0.5 hPa) with high vertical resolution (~1 km). These continuous observations at one azimuth can facilitate studies on short-lived processes (e.g., gravity waves (Alexander et al., 2008)) and possibly TFs. Because of this failure, HIRDLS is not able to measure the same atmospheric column within 15 min as the rest Aura instruments, but instead views the same location 84 min earlier than MLS at night and 17° to the east of the MLS track during the daytime.

We use version 5 (v5.00.00) HIRDLS ozone data in this study. The data with negative "O3Precision" or earthward from the nearest and above the "CloudTopPressure" are screened out. The "gradient filter" is not applied, because high vertical ozone gradient exists when tropopause folds occur. Note that without "gradient filter" some unrealistically high ozone spikes may not be excluded (see Figs. 3g and 4g).

4.2 MLS

MLS measures stratospheric and upper tropospheric ozone using microwave limb sounding technology at 240 GHz (Schoeberl et al., 2006; Waters et al., 2006). Although the version 3.3 standard O_3 product has doubled vertical resolution and enlarged pressure range, we opt here for version 2.2 data, as oscillations appear in the tropical upper troposphere (UT) profiles of version 3.3, even for monthly mean ozone profiles (Livesey et al., 2011). The vertical resolution of MLS ozone profiles is ~3 km in the UT and stratosphere. The horizontal resolution is ~200 km×6 km (along-track × cross-track) (Livesey et al., 2007). We extract the scientifically useful data from 215 hPa to 0.02 hPa. Only the data with (1) positive precision, (2) even-numbered "Status", (3) "Quality" greater than 1.2, and (4) "Convergence" less than 1.8 are used in this study.

ACPD
11, 26897–26941, 2011

4.3 OMI

OMI uses a 2-dimensional Charge-Coupled Device to measure the backscattered solar irradiance from nadir direction at ultraviolet and visible wavelengths (UV-1: 264–311 nm, UV-2: 307–383 nm, VIS: 349–504 nm). The wide cross-orbit swath (2600 km) allows OMI to provide global daily coverage (OMI Team, 2009). In this study, we use the OMO3PR V003 ozone profiles with a horizontal resolution of 13 km×48 km (along-track × cross-track) and 18 vertical layers from the surface to 0.3 hPa (de Haan and Veefkind, 2009). In the troposphere, the vertical resolution is very coarse (3–6 layers) and thus OMI cannot resolve vertical structures such as TFs. OMI does provide useful information about the tropospheric column, including its enhancements in regions with TFs (Tang and Prather, 2010). The OMI tropospheric column ozone (TCO) is derived by applying the tropopause height output from the UCI CTM to the ozone profiles.

4.4 TES

TES is a high resolution infrared Fourier transform spectrometer with spectral coverage from 650 to 3250 cm^{-1} at a spectral resolution at 0.025 cm^{-1}. It is designed to view the atmosphere in both nadir and limb directions with a 5 km×8 km nadir footprint. The limb scan mode, however, was eliminated in 2005 to conserve instrument life. The version 4 (V004, F05_07) nadir global survey standard ozone product is used in this paper. The profiles are reported at 67 pressure levels from the surface to 0.1 hPa. Ozone profiles whose "SpeciesRetrievalQuality" or "O3_Ccurve_QA" does not equal to 1 are excluded (Osterman et al., 2009). Some of the TES profiles (0.5 %) contain fill values for the averaging kernel (AK), and these are also excluded.

ACPD
11, 26897–26941, 2011

4.5 Methods of mapping modeled ozone profiles onto reported Aura measurements

The CTM and Aura ozone profiles all have different locations and pressure coordinates. In terms of geographic collocation, we pick the 1°×1° model grid without interpolation that the centre (for OMI and TES) or the location of the tangent height (for HIRDLS and MLS) of the observation falls in. Temporal values are interpolated between the two half-hour model simulations bounding the observation as described above. The vertical remapping is more complex and specific to each instrument. Before comparing them, we first map CTM profiles onto the Aura levels either by linear interpolation in pressure for HIRDLS and MLS or by convolution with the a priori and averaging kernel (AK) (together referred as the satellite operator) for OMI and TES. The "least squares fit" method, recommended by Livesey et al. (2007), is unstable for the lower most a few MLS layers, which are particularly important for this paper. Also considering that HIRDLS and MLS have vertical resolutions comparable to that of the CTM, we decided to simply interpolate the CTM profiles onto HIRDLS and MLS levels. For OMI and TES the satellite operators are applied on the CTM profiles to account for limited vertical resolution and sensitivity of nadir viewing measurements based upon the following equation (e.g., Luo et al., 2007; Worden et al., 2007):

$$\hat{\boldsymbol{x}}_{\mathrm{m}} = \boldsymbol{x}_{\mathrm{a}} + \mathbf{A}(\boldsymbol{x}_{\mathrm{m}} - \boldsymbol{x}_{\mathrm{a}}) \quad (1)$$

where $\boldsymbol{x}_{\mathrm{a}}$ and $\mathbf{A}$ are the a priori and averaging kernel reported in every OMI and TES HDF-EOS5 metadata. The modeled ozone profiles are first interpolated onto the satellite levels. The above equation then transforms the interpolated profiles $\boldsymbol{x}_{\mathrm{m}}$ to the "retrieved" profiles $\hat{\boldsymbol{x}}_{\mathrm{m}}$, mimicking the vertical smoothing of the retrieval process of OMI and TES data. Note that $\boldsymbol{x}_{\mathrm{m}}$ is in Dobson Unit (DU) for OMI and the natural logarithm of ozone molar ratio for TES.

ACPD
11, 26897–26941, 2011

4.6 Problems with applying satellite operators for nadir-view instruments

Convolving modeled or sonde profiles with Eq. (1) essentially smoothes those profiles vertically and relaxes them towards the retrieval a priori. For most regions, this method works adequately and smoothes the profiles as expected. In the UT, however, the satellite operator can cause unphysically high biases (see Fig. 1a and Table 1). Figure 1a shows the comparison for one of the TES profiles in Fig. 4i at 9.5° S, 295.0° E. The TES profile (red line) contains a slight inversion at 630 hPa, determined mainly by its a priori (green line), and a dispersed fold at 600–200 hPa that is primarily contributed by the TES signal. From 120 hPa to 70 hPa, TES values are almost identical to a priori values. The linearly interpolated CTM profile (blue line) also resolve the two folds but shows folds with larger magnitudes. The modeled profile matches the shape as well as the magnitude of TES in the UT. With the TES operator, the CTM profile (black line) still has the fold at 630 hPa, but the vertical gradient becomes smoother and the shape is quite similar to the a priori estimate. However, the fold at 400 hPa is totally smoothed out and the ozone abundance increases monotonically above 400 hPa with much larger slope than that of TES a priori or TES or the raw model profile in the UT, resulting in up to a factor of 2 larger values for the "TES-processed" model compared to TES in this area. Smearing stratospheric information down to the troposphere by the TES retrieval process is also noted by other studies (e.g., Osterman et al., 2008).

The artificial high bias in the UT introduced by the TES operator reflects TES's coarse vertical resolution around the tropopause and the large cross-tropopause ozone gradient. The AK for this particular measurement shown in Fig. 1b, is generally wide, indicating coarse vertical resolution. Despite reporting data at 67 levels, the degrees of freedom for the signal (DOFS), which is the trace of the AK, of this measurement are 0.5, 1.5 and 4.0 for the UT (250–100 hPa), the troposphere, and all the levels, respectively. In other words, the TES values at different levels are highly correlated. The layers at 100–50 hPa and 400–250 hPa have contribution factors to the 250–100 hPa layer that range from the same to twice as large as the layer itself (red lines in Fig. 1b).

ACPD
11, 26897–26941, 2011

Therefore, the large differences between the TES a priori (green line in Fig. 1a) and the raw model profile (blue line in Fig. 1a) in the stratosphere are smoothed and aliased into the UT, swamping the clear UT signal in the model, and leading to the high model biases in this region.

Table 1 shows the means, standard deviations (σ), and the root mean squares (RMS) of the partial columns for the TES and the corresponding CTM profiles of the swath shown in Fig. 4i. This swath consists of 54 individual profiles, covering 31.5° S–71.4° N. In the upper troposphere (400 hPa–tropopause (TPP)), the raw CTM mean (second column) is 7 % smaller than TES (fourth column). After processing with the TES operator, the CTM value (third column) is enhanced by 3.0 DU (almost 1σ) and becomes 14 % larger than TES. In the middle (700–400 hPa) and lower (surface–700 hPa) troposphere with the TES operator, the model means become smaller and closer to the TES means. The RMS of anomalies (column 5 and 6) is increased by the operator in the UT, while reduced in middle and lower troposphere.

The results in Table 1 are typical and suggest that the TES operator cause artificial high biases in the UT over most latitudes, which is also true for OMI, whose vertical resolution is even coarser than TES. One possible solution for this problem is to redo the TES retrieval process using our modeled profiles as the a priori and compare the output with the existing TES data, but this would be an extensive effort beyond the scope of this paper. Because the UT region is greatly affected by the STE processes (e.g., Terao et al., 2008), on which this paper focuses, we decided to compare the interpolated CTM profiles directly with TES on TES pressure levels in the following case studies (Sect. 6.1), and we show results both with and without the TES operator for the rest analysis. This is a general problem when using satellite operators. It highlights the fact that to avoid misusing and/or misinterpreting satellite data, it is important to know the sensitivities and resolutions of satellite measurements, especially in regions with large gradients like the tropopause.

The artificial high bias of the nadir satellite operators in the UT however, appears to have only a small effect on the tropospheric column ozone (TCO) as shown by the

ACPD
11, 26897–26941, 2011

sums of the second and third columns (38.0 DU vs. 38.1 DU) of Table 1. The TES DOFS in the troposphere is generally greater than one (Zhang et al., 2010) and thus gives reasonable TCO values. Likewise, OMI has approximately one DOFS for the troposphere (de Haan and Veefkind, 2009), and its TCO matches the simulation in terms of geographical patterns and magnitudes (Tang and Prather, 2010). Therefore, when comparing the TCO of TES or OMI with the model results, we process the CTM profiles with satellite operators.

5 Temporal and spatial scales of STE

The knowledge about the temporal and spatial scales of STE related processes is important for investigating stratospheric ozone influx. Figure 2 illustrates the high variability of STE flux by three snapshots of simulated ozone cross sections as a function of pressure altitude ($z^*\text{km} = 16 \times \log_{10}(1000/p\,\text{hPa})$) and longitude at 29.4° N starting on 31 January 2005 at 00:00 UTC with a 2-h interval. The tropopause folding structures, outlined by the thick black lines for O_3 abundances of 100-ppb (parts per billion, nanomoles per mole of air) suggest cross-tropopause mixing. The magenta squares mark the same CTM grid box and highlight the short-lived feature of tropopause folds. In Fig. 2a, the magenta box is located in the stratospheric part of a TF beneath an isolated tropospheric air parcel (may be connected with the troposphere in 3-D). Two hours later, another TF develops and its tropospheric branch extends over the box (Fig. 2b). The isolated tropospheric parcel in Fig. 2a reconnects with the tropospheric air at ∼10° east in Fig. 2b. The folds continue moving to the east and the box is occupied by the troposphere after another two hours (Fig. 2c). An isolated stratospheric parcel (140° E) and tropospheric parcel (170° E) also emerge at 12–14 km in Fig. 2c. An isolated stratospheric parcel stays in deep troposphere (130–150° E, 6–8 km) with little changes in the 6-h time frame, indicating a significant stratospheric intrusion and showing that the STE process can be relatively long-lived. Given the objective of identifying TFs, we must compare with the Aura level 2 (L2) swath data instead of the level

ACPD
11, 26897–26941, 2011

3 (L3) gridded data that are averaged over two weeks or more. Figure 2 also indicates that the STE processes occur on the scale of a few hundred kilometers and require model resolutions of about 1° to match the observations.

6 Results

6.1 Case studies

We pick our case studies of tropopause folds as follows: an ozone sonde observes a folding event; the OMI swath overlaps the sonde measurement within one hour; and all four Aura measurements are available. Out of the 1907 WOUDC ozone sondes and ~10 thousand Aura swaths, there are eight such cases in year 2005. Two of these cases are shown in Figs. 3 and 4 here, while the remaining six are in the appendix (Figs. A1–A6). In Fig. 3, the sonde profile is measured at Hong Kong (22.3° N, 114.2° E, station code 344) on 23 March 05:26 UTC and the Aura and CTM swaths are for 05:00–06:00 UTC. The case in Fig. 4 shows the sonde at Wallops Island (37.9° N, 75.5° W, station code 107) for 25 August 17:39 UTC and Aura and CTM swaths for 18:00–19:00 UTC.

The modeled ozone profiles (red line) are compared with the sondes (blue line) in Figs. 3a and 4a. The CTM profiles are from the 1°×1° grid boxes containing the sonde stations and temporally closest in the 2-h output field (06:00 UTC for Fig. 3a and 18:00 UTC for Fig. 4a). In the first case, the model and sonde have the same main shape (Fig. 3a): ozone decreases with height in the boundary layer (1000–800 hPa), and increases in the free troposphere with a clear significant inversion in the upper troposphere and another one of smaller magnitude at 125 hPa. The CTM misses the high values around 700 hPa. The simulated profile has larger variance in the free troposphere. The middle troposphere maximum seen in the sonde (300–200 hPa) occurs lower in the CTM (400–300 hPa) and is attributable to a TF. The model slightly underestimates the folding at 125 hPa. In the second case, the model precisely reproduces the

ACPD
11, 26897–26941, 2011

magnitude of the folding structure at 300 hPa with the peak point about 30 hPa lower in altitude, but overestimates the variance at the tropopause (120 hPa, Fig. 4a). These two comparisons reveal that the model generally matches the sonde in the shape and magnitude, in particular resolving folds, and give us some confidence that the model is capable of reproducing the folding structures and patterns in the nearly concurrent Aura swaths.

The locations of each available Aura measurement (HIRDLS: black crosses, MLS: cyan crosses, OMI: green dots, TES: red crosses) in the one hour period close to the sonde measurement are shown on the CTM grids in Figs. 3b and 4b. Note that although the swaths of MLS and TES nearly overlap, MLS measurements are a few minutes ahead of TES as MLS performs forward limb scan, whereas TES views in nadir direction. Only OMI and TES can have exactly matching measurements in both time and location. The large black crosses represent the sonde locations. The comparisons between Aura and simulated swaths are resented in Figs. 3c, 4c vs. Figs. 3d, 4d for OMI, Figs. 3e, 4e vs. Figs. 3f, 4f for MLS, Figs. 3g, 4g vs. Figs. 3h, 4h for HIRDLS, and Figs. 3i, 4i vs. Figs. 3j, 4j for TES. Each Aura measurement is compared with the coincident model result for the grid box containing the centre of the Aura observation. The modeled profiles are interpolated onto the corresponding Aura levels for the comparisons. The white spaces in the Aura swaths (panels c, e, g, i of Figs. 3 and 4) are either no measurements or bad values. The CTM swaths, on contrast, consist of all the profiles along the orbit to demonstrate the full picture. The white areas in Figs. 3j and 4j reflect the topography. The black lines imposed on the vertical swaths represent the tropopause at each measurement location as determined by the artificial tracer e90 in the CTM (Prather et al., 2011). For OMI, we compare the TCO as a function of latitude and longitude, since OMI only contain one degree of freedom for the signal in the troposphere (de Haan and Veefkind, 2009). For the remaining three Aura instruments, the comparisons are performed for the altitude-by-latitude cross-sections of each swath for 0–180° E in Fig. 3 and 180–360° E in Fig. 4.

ACPD
11, 26897–26941, 2011

The model simulates the OMI TCO swath quite well (see Fig. 3c, d and Fig. 4c, d) as previously shown by Tang and Prather (2010). Here, the CTM profiles are convolved with the OMI operator to account for the limited vertical resolution and sensitivity of OMI, whereas Tang and Prather (2010) use the raw modeled profiles. The OMI TCO uses the tropopause height calculated by the CTM to make consistent comparisons. The convolution does not have great impact on the CTM TCO. In Fig. 3c, d, the high columns appear over Northern and Eastern Asia as well as Australia in both OMI and the CTM. The geographic patterns match in details, such as the curvature in Northern Asia. The OMI TCO swath contains more high-frequency variability, likely to be noise, than does the CTM. Figure 4c, d show similar results. Both the model and OMI have high TCO over North and South America. The CTM, however, underestimates TCO over North America and overestimates it over South America. The biases are within ±5 DU. The high anomalies in TCO are correlated with TF events, particularly near the subtropical jet streams (Tang and Prather, 2010) and hence can provide clues about whether the folding structures in MLS and TES swaths are realistic.

MLS and the CTM have consistent latitudinal gradient of tropopause height with the typical lower stratospheric values (>200 ppb) at 68 hPa in the tropics and 215 hPa in the extra-tropics. In terms of O_3, the tropics-to-midlatitude transition from troposphere to stratosphere is the same in both: 23° S at 100 hPa and 30° N at 215 hPa in Fig. 3e, f; and 18° N at 100 hPa and 60° N at 215 hPa in Fig. 4e, f. MLS reports inversion structures near 13° S at 147–100 hPa (Fig. 3e), which are not found in the modeled swath (Fig. 4e). The corresponding OMI and CTM TCO do not show high anomalies around 13° S, and thus these inversions in the MLS data are probably noise in the MLS retrieval procedure. The folding structures at 15° N–30° N are consistent in MLS and CTM swaths and confirmed by the TCO high anomalies. Some unphysical values emerge in the MLS data with no analogues in the model, such as >200 ppb O_3 at 215 hPa near the equator, 70 ppb at 68 hPa at 20° N (Fig. 3e), and >200 ppb at 147 hPa at 12° N (Fig. 4e).

ACPD
11, 26897–26941, 2011

For HIRDLS, most of the tropospheric values are missing for the tropics (Figs. 3g and 4g). The tropopause region in HIRDLS swaths appears more fuzzy and diffused with some non-physical, low values (<50 ppb) in the stratosphere (e.g., 17° N at 70 hPa in Fig. 3g) and unrealistical, high values (>200 hPa) in the troposphere (e.g., 7° N at 130 hPa and 10° S at 196 hPa in Fig. 4g). These unphysical numbers reflect the fundamental difficulty with HIRDLS or any limb scanning instrument of quantifying ozone abundances as they decline repidly below the tropopause. Some of the non-physical, high abundances may be screened out as "high spikes" (HIRDLS Team, 2010). On the other hand, HIRDLS does observe some tropospheric patterns that are consistent with the simulation, such as the high-O_3 spot at 150 hPa near 30° N in Fig. 3g and the low values at 230 hPa near 21° N in Fig. 4g. Given the fine vertical resolution (~1 km), HIRDLS can resolve major STE events, following stratospheric air well into the troposphere (see Pan et al., 2009, for a case on 11 May 2007), but we did not find these in our test cases for 2005–2006.

Observing at nadir angles, TES is able to retrieve the ozone profile down to the ground, but the vertical resolution is much coarser than MLS, HIRDLS, and the CTM in the UT/LS region. The profiles in the TES swaths (Figs. 3i and 4i) are much smoother compared to the CTM simulation, catching the main components and patterns but missing most of the details. In Fig. 3i, j, both TES and the CTM display high ozone abundances about 20° N at 631 hPa and 42° N at 400 hPa plus the displacement of stratospheric air (with O_3>200 ppb) down to a typical troposphere regime (38–50° N, 400–250 hPa), indicating stratospheric intrusions. The locations of these intrusions match the cyclonic pattern in observed and simulated OMI swaths (Fig. 3c, d). TES, however, mismatches the intrusion structures at 20° N at 280 and 158 hPa. In Fig. 4i, j, high O_3 (~80 ppb) values are found near 10° S at 350 hPa in both TES and the CTM, but the hot spot at 700 hPa at that latitude, probably due to biomass burning, is seen only in the CTM. TES senses the high anomaly at 37° N near the surface, showing some skill in detecting boundary-layer O_3. The enhanced ozone at 15° N 400 hPa is consistent for both. The tropospheric inversion patterns simulated by the CTM at 30–60° N are seen

ACPD
11, 26897–26941, 2011

as a broad area of enhanced O_3 by TES.

The other six cases (Figs. A1–A6) show very similar results as the above two cases for different locations and time. In one case (Fig. A2, 6 July 2005) the CTM reproduces the large stratospheric fold at 200 hPa as seen by the sonde, and the MLS and the CTM patterns match quite well in Fig. A2e, f, except for the magnitudes of a few points. HIRDLS observes a stratospheric intrusion at 45° N, 260–200 hPa, also in agreement with the model. In anther case (Fig. A4, 3 August 2005) TES matches the intrusion patterns of the CTM at 25° S–10° S, 630–160 hPa and at 40° N–50° N, 450–250 hPa. In Fig. A6 (19 December 2005) TES and the CTM basically agree on the intrusion patterns at 20° N, 400–150 hPa as well as the high O_3 area at 19° S–5° S, 630–400 hPa, although the TES pattern is more diffuse and lower in altitude.

Olsen et al. (2008) found an intrusion within the stratosphere from the tropics to high latitudes in the HIRDLS data in 26 January 2006. Figure A7 presents this case in the same way as the above eight cases except that there is no sonde available and the color scale is adjusted to emphasize the stratosphere with a range of 0–5 ppm. In the newer version (v5.00.00) of HIRDLS data, the intrusion is also found near 100 hPa at 30–55 N with about 2 km thick (80–110 hPa) (see Fig. A7g). Figure A7h simulates this low O_3 layer at the same location, but the O_3 abundance in the surrounding air biases high relative to the HIRDLS measurements due to the stratospheric circulation problems of the 40-layer ECMWF meteorological fields (Hsu and Prather, 2009) driving the CTM. The MLS swath (Fig. A7e) indicates an inversion structure at 52° N, 100 hPa, which does not appear in the simulation (Fig. A7f).

These cases studies of the five Aura ozone measurements and the CTM simulations, made on an instantaneous basis, confirm the model's ability of reproducing the STE processes and show that the Aura measurements can detect some of the fine structures in O_3, such as TFs and stratospheric intrusions deep into the troposphere, while they miss a large number of such cases, presumably due to the noise in individual measurements. The Aura datasets are therefore capable of mapping individual TFs and the STE process only for a few specific cases (e.g., Olsen et al., 2008; Pan

ACPD
11, 26897–26941, 2011

et al., 2009; Manney et al., 2011), and cannot provide observations of all the individual events that could lead to a general, comprehensive integration of the global STE flux.

6.2 CTM vs. Aura instantaneous comparisons

The observations of the three Aura ozone profilers – HIRDLS, MLS, and TES – do not coincide each other. They do not look at the same air mass at the same time and have dramatically different profiling techniques. From the point of view of using the Aura observations to map out rapidly changing tropopause folds and stratospheric intrusions, we need a 4-D description of atmospheric O_3 to determine if these instruments are measuring the same ozone. In this section, we use the UCI CTM as an intercomparison platform to study the consistency amongst the Aura ozone datasets focusing on the UT/LS regions.

The 2-D probability density functions (PDFs) of the CTM vs. MLS, HIRDLS, and TES are shown for July 2005 and January 2006 at 215 hPa and 147 hPa in Figs. 5–8. These PDFs include every exact-match, CTM-Aura pair for five latitude zones: NH middle latitude (40° N–50° N), NH jet (25° N–35° N), tropics (15° S–15° N), SH jet (35° S–25° S), and SH middle latitude (50° S–40° S). For TES, we present the comparisons for both the raw CTM simulation (fourth column) and that convolved with the TES operator (third column). The PDF (units of frequency per ppb^2) is weighted inversely by the sampling times for each latitude to account for unequal observations from different latitudes, and it is normalized for a 2-D integral of 1. The number of CTM-Aura matches for the month are shown on each panel.

The red, high-density pixels are generally located close to the black solid, 1:1 line for all the three instruments, indicating small biases, except for stratospheric comparisons such as Fig. 6q–t. The CTM is generally biased high compared to all three Aura measurements in the LS, suggesting a model deficiency that is most likely due to the errors in the stratospheric circulation of the 40-layer ECMWF meteorological fields (Hsu and Prather, 2009). As expected, TES gives generally tighter PDFs than MLS and HIRDLS, reflecting the differences in nadir and limb scanning. For tropospheric model

ACPD
11, 26897–26941, 2011

values (<100 ppb), such as in the tropics and jet regions of the summer hemisphere (Fig. 5e, f, i, j), the slopes of MLS and HIRDLS PDF are almost flat, suggesting low sensitivities and great noise in bottom layers of these limb scanning measurements. Negative MLS profile values (e.g., Fig. 5a–q) are allowed in the retrieval algorithm to achieve the correct column loading (Livesey et al., 2007). The PDFs of HIRDLS are notably more dispersed compared to those of MLS and TES at 215 hPa for the winter hemisphere middle latitudes (Fig. 5r, and Fig. 7b), indicating HIRDLS difficulties for this region and season. With the TES operator, the tropospheric CTM values (<100 ppb) are enhanced to stratospheric levels (>100 ppb) (e.g., Fig. 5c vs. d, and Fig. 7s vs. t) as previously shown in Sect. 4.6. The CTM-TES comparisons are almost always improved with application of the TES averaging kernel (e.g., Fig. 5g vs. h, and Fig. 8g vs. h) due to the relaxing towards the TES a priori and reducing the variance at a given pressure level by vertical smoothing (see Tables 2 and 3). Without some clear indication of the relative influence of the a prior in each retrieval, this CTM-TES agreement may be artificial.

Tables 2 and 3 summarize the mean biases and root mean square (RMS) errors for Figs. 5–8. The RMS errors are generally much larger than the biases, consistent with previous validations against ozone sondes (e.g., Jiang et al., 2007; Nassar et al., 2008; Zhang et al., 2010), and most likely due to the high variability at this pressure range for all latitude zones in both summer and winter. Note that the biases are less meaningful given such large RMS and thus the biases are only good for qualitative, long-term averages (i.e., L3 monthly gridded data). The biases clearly show the CTM overestimates in subtropical jet and mid-latitude regions, again supporting a model deficiency in these regions.

The results in Tables 2 and 3 also imply inconsistencies among the Aura datasets. In July 2005 at 215 hPa, the CTM means are smaller than MLS and TES, while greater than HIRDLS in the tropics and NH jets and mid-latitudes. Comparisons with sonde show a less than 15 % positive bias of TES (Nassar et al., 2008; Richards et al., 2008) in the troposphere and ~20 % high bias of MLS at the middle to high latitudes at

ACPD
11, 26897–26941, 2011

215 hPa (Jiang et al., 2007). Thus, we have easily demonstrated that HIRDLS has large positive biases of ~30–100 ppb at 215 hPa for summer from the tropics to NH mid-latitudes. In the tropics at 147 hPa, the CTM is smaller than MLS and HIRDLS but larger than TES for both July 2005 and January 2006, identifying a clear discrepancy between MLS-HIRDLS and TES without having to find collocated observations. We note that the RMS is much larger than the mean biases although the standard error of the mean (SEM) calculated assuming a normal distribution is smaller. The bias clearly does not show in individual measurements, and the statistical significance of the bias in L3 gridded data depends greatly on the assumption of a normal error that does not depend systematically on specific atmospheric conditions.

7 Conclusions

The high-resolution CTM (1°×1°×40-layer×0.5 h) simulation of ozone reveals that the time scale of stratosphere-troposphere exchange (STE) processes observed at a given location is as short as hours and indicates that STE occurs on a spatial scale of a few hundred kilometers. For nadir-view instruments (e.g., TES and OMI), the application of their satellite operators (averaging kernel (AK) and a priori) can cause artificial high bias in the upper troposphere, as the nadir-view measurements have coarse vertical resolutions and their AK smears the stratospheric, high O_3 abundance into the troposphere.

The Aura L2 swath data are chosen to study the STE flux of ozone based upon the short-lived features of most STE processes. The high-resolution simulation with the UCI CTM depicts the full ozone picture for year 2005–2006 to compare with the individual, non-coincident Aura ozone measurements (except for OMI and TES) derived from different remote sensing techniques. The model's ability of reproducing STE-related processes, such as tropospheric folds (TF), is confirmed by the comparisons with WOUDC sondes, which gives confidence on the reliability and accuracy of the folding and intrusion structures simulated instantaneously for the cross sections along

ACPD
11, 26897–26941, 2011

Aura swaths.

From eight cases studies, all four Aura instruments demonstrate some skill in catching the STE structures, either from the high TCO anomalies (for OMI) or from the O_3 vertical profiles (for HIRDLS, MLS, and TES), despite missing many of them. Tropopause folds and stratospheric intrusions of O_3 present a fundamental difficulty for satellite passive remote sensing due to large abundances and columns of stratospheric ozone above the troposphere. Aura datasets have been useful for only a few STE case studies, such as Olsen et al. (2008); Pan et al. (2009); Manney et al. (2011). Improvements in the instruments and sensing techniques so as to greatly reduce the apparent noise in individual retrievals will be necessary if satellite observations are to be used to map out folds and intrusions and thus provide better constrains for the STE modeling.

We use the CTM as an intercomparison platform to investigate the consistency of different Aura ozone measurements. The CTM deficiencies can be readily identified when the biases are similar against all Aura observations. The 2-D PDF as well as the mean biases and RMS of exact matching CTM-Aura comparisons for five latitude bins identifies the model's high biases in the lower stratosphere due most likely to the problems in the stratospheric circulation. On the other hand, the CTM as a transfer standard can be used to identify clearly the relative biases in the Aura ozone instruments on an instantaneous basis, even when they do not have overlapping measurements. It also can help decide which of those measurements are in error. Different signs of model-measurement biases for HIRDLS, MLS, and TES are found from tropics to NH mid-latitudes in July 2005 at 215 hPa and over tropics at 147 hPa for July 2005 and January 2006, identifying the inconsistency across these Aura datasets.

ACPD
11, 26897–26941, 2011

Appendix A Other case study results

The other case studies are shown in Figs. A1–A7.

Acknowledgements. This work is funded by NASA grant (NNX08AR25G) to UCI.

References

Alexander, M. J., Gille, J., Cavanaugh, C., Coffey, M., Craig, C., Eden, T., Francis, G., Halvorson, C., Hannigan, J., Khosravi, R., Kinnison, D., Lee, H., Massie, S., Nardi, B., Barnett, J., Hepplewhite, C., Lambert, A., and Dean, V.: Global estimates of gravity wave momentum flux from High Resolution Dynamics Limb Sounder observations, J. Geophys. Res., 113, D15S18, doi:10.1029/2007JD008807, 2008. 26902

Atkinson, R. and Arey, J.: Gas-phase tropospheric chemistry of biogenic volatile organic compounds: a review, Atmos. Environ., 37, 197–219, doi:10.1016/S1352-2310(03)00391-1, 2003. 26898

Carver, G., Brown, P., and Wild, O.: The ASAD atmospheric chemistry integration package and chemical reaction database, Comput. Phys. Commun., 105, 197–215, 1997. 26900

Danielsen, E. F.: Stratospheric-tropospheric exchange based on radioactivity, ozone and potential vorticity, J. Atmos. Sci., 25, 502–518, 1968. 26899

de Haan, J. F. and Veefkind, J. P.: OMO3PR Readme, available online at: http://disc.sci.gsfc.nasa.gov/Aura/data-holdings/OMI/documents/v003/OMO3PRO_README.html, 2009. 26903, 26907, 26909

Denman, K. L., Brasseur, G., Chidthaisong, A., Ciais, P., Cox, P. M., Dickinson, R. E., Hauglustaine, D., Heinze, C., Holland, E., Jacob, D., Lohmann, U., Ramachandran, S., da Silva Dias, P. L., Wofsy, S. C., and Zhang, X.: Couplings Between Changes in the Climate System and Biogeochemistry, in: Climate Change 2007: The Physical Science Basis. Contribution of Working Group I to the Fourth Assessment Report of the Intergovernmental Panel on Climate Change, edited by Solomon, S., Qin, D., Manning, M., Chen, Z., Marquis, M., Averyt, K. B., Tignor, M., and Miller, H. L., Cambridge University Press, Cambridge, UK and New York, NY, USA, chap. 7, 499–587, 2007. 26899

Fusco, A. C. and Logan, J. A.: Analysis of 1970–1995 trends in tropospheric ozone at North-

ACPD

11, 26897–26941, 2011

ern Hemisphere midlatitudes with the GEOS-CHEM model, J. Geophys. Res., 108, 4449, doi:10.1029/2002JD002742, 2003. 26898

Gauss, M., Myhre, G., Isaksen, I. S. A., Grewe, V., Pitari, G., Wild, O., Collins, W. J., Dentener, F. J., Ellingsen, K., Gohar, L. K., Hauglustaine, D. A., Iachetti, D., Lamarque, F., Mancini, E., Mickley, L. J., Prather, M. J., Pyle, J. A., Sanderson, M. G., Shine, K. P., Stevenson, D. S., Sudo, K., Szopa, S., and Zeng, G.: Radiative forcing since preindustrial times due to ozone change in the troposphere and the lower stratosphere, Atmos. Chem. Phys., 6, 575–599, doi:10.5194/acp-6-575-2006, 2006. 26898

Gettelman, A., Holton, J. R., and Rosenlof, K. H.: Mass fluxes of O_3, CH_4, N_2O and CF_2Cl_2 in the lower stratosphere calculated from observational data, J. Geophys. Res., 102, 19149–19159, doi:10.1029/97JD01014, 1997. 26899

HIRDLS Team: High Resolution Dynamics Limb Sounder Earth Observing System (EOS) Data Description and Quality Version 5 (V5), available online at: http://disc.sci.gsfc.nasa.gov/Aura/data-holdings/HIRDLS/documents/HIRDLS-V5-DQD-6May2010.pdf, last access: 10 May 2010, 2010. 26902, 26911

Holmes, C. D., Tang, Q., and Prather, M. J.: Uncertainties in climate assessment for the case of aviation NO, P. Natl. Acad. Sci. USA, 108, 10997–11002, doi:10.1073/pnas.1101458108, 2011. 26898

Hoor, P., Borken-Kleefeld, J., Caro, D., Dessens, O., Endresen, O., Gauss, M., Grewe, V., Hauglustaine, D., Isaksen, I. S. A., Jöckel, P., Lelieveld, J., Myhre, G., Meijer, E., Olivie, D., Prather, M., Schnadt Poberaj, C., Shine, K. P., Staehelin, J., Tang, Q., van Aardenne, J., van Velthoven, P., and Sausen, R.: The impact of traffic emissions on atmospheric ozone and OH: results from QUANTIFY, Atmos. Chem. Phys., 9, 3113–3136, doi:10.5194/acp-9-3113-2009, 2009. 26898, 26901

Hsu, J. and Prather, M. J.: Stratospheric variability and tropospheric ozone, J. Geophys. Res., 114, D06102, doi:10.1029/2008JD010942, 2009. 26898, 26899, 26900, 26912, 26913

Hsu, J., Prather, M. J., and Wild, O.: Diagnosing the stratosphere-to-troposphere flux of ozone in a chemistry transport model, J. Geophys. Res., 110, D19305, doi:10.1029/2005JD006045, 2005. 26899

Isaksen, I. S. A., Zerefos, C., Kourtidis, K., Meleti, C., Dalsoren, S. B., Sundet, J. K., Grini, A., Zanis, P., and Balis, D.: Tropospheric ozone changes at unpolluted and semipolluted regions induced by stratospheric ozone changes, J. Geophys. Res., 110, D02302, doi:10.1029/2004JD004618, 2005. 26900

ACPD
11, 26897–26941, 2011

Jiang, Y. B., Froidevaux, L., Lambert, A., Livesey, N. J., Read, W. G., Waters, J. W., Bojkov, B., Leblanc, T., McDermid, I. S., Godin-Beekmann, S., Filipiak, M. J., Harwood, R. S., Fuller, R. A., Daffer, W. H., Drouin, B. J., Cofield, R. E., Cuddy, D. T., Jarnot, R. F., Knosp, B. W., Perun, V. S., Schwartz, M. J., Snyder, W. V., Stek, P. C., Thurstans, R. P., Wagner, P. A., Allaart, M., Andersen, S. B., Bodeker, G., Calpini, B., Claude, H., Coetzee, G., Davies, J., Backer, H. D., Dier, H., Fujiwara, M., Johnson, B., Kelder, H., Leme, N. P., König-Langlo, G., Kyro, E., Laneve, G., Fook, L. S., Merrill, J., Morris, G., Newchurch, M., Oltmans, S., Parrondos, M. C., Posny, F., Schmidlin, F., Skrivankova, P., Stubi, R., Tarasick, D., Thompson, A., Thouret, V., Viatte, P., Vömel, H., von Der Gathen, P., Yela, M., and Zablocki, G.: Validation of Aura Microwave Limb Sounder Ozone by ozonesonde and lidar measurements, J. Geophys. Res., 112, D24S34, doi:10.1029/2007JD008776, 2007. 26914, 26915

Kraabøl, A. G., Berntsen, T. K., Sundet, J. K., and Stordal, F.: Impacts of NO_x emissions from subsonic aircraft in a global three-dimensional chemistry transport model including plume processes, J. Geophys. Res., 107, 4655, doi:10.1029/2001JD001019, 2002. 26900

Lacis, A. A., Wuebbles, D. J., and Logan, J. A.: Radiative Forcing of Climate by Changes in the Vertical Distribution of Ozone, J. Geophys. Res., 95, 9971–9981, doi:10.1029/JD095iD07p09971, 1990. 26899

Livesey, N. J., Read, W. G., Lambert, A., Cofield, R. E., Cuddy, D. T., Froidevaux, L., Fuller, R. A., Jarnot, R. F., Jiang, J. H., Jiang, Y. B., Knosp, B. W., Kovalenko, L. J., Pickett, H. M., Pumphrey, H. C., Santee, M. L., Schwartz, M. J., Stek, P. C., Wagner, P. A., Waters, J. W., and Wu, D. L.: Earth Observing System (EOS) Aura Microwave Limb Sounder (MLS) Version 2.2 Level 2 data quality and description document, Tech. Rep. D-33509, JPL, Jet Propulsion Laboratory California Institute of Technology Pasadena, California, 91109-8099, 2007. 26902, 26904, 26914

Livesey, N. J., Read, W. G., Froidevaux, L., Lambert, A., Manney, G. L., Pumphrey, H. C., Santee, M. L., Schwartz, M. J., Wang, S., Cofield, R. E., Cuddy, D. T., Fuller, R. A., Jarnot, R. F., Jiang, J. H., Knosp, B. W., Stek, P. C., Wagner, P. A., and Wu, D. L.: Earth Observing System (EOS) Aura Microwave Limb Sounder (MLS) Version 3.3 Level 2 data quality and description document, Tech. Rep. D-33509, JPL, Jet Propulsion Laboratory California Institute of Technology Pasadena, California, 91109-8099, 2011. 26902

Luo, M., Rinsland, C., Fisher, B., Sachse, G., Diskin, G., Logan, J., Worden, H., Kulawik, S., Osterman, G., Eldering, A., Herman, R., and Shephard, M.: TES carbon monoxide validation with DACOM aircraft measurements during INTEX-B 2006, J. Geophys. Res., 112, D24S48,

ACPD
11, 26897–26941, 2011

doi:10.1029/2007JD008803, 2007. 26904
Manney, G. L., Hegglin, M. I., Daffer, W. H., Santee, M. L., Ray, E. A., Pawson, S., Schwartz, M. J., Boone, C. D., Froidevaux, L., Livesey, N. J., Read, W. G., and Walker, K. A.: Jet characterization in the upper troposphere/lower stratosphere (UTLS): applications to climatology and transport studies, Atmos. Chem. Phys., 11, 6115–6137, doi:10.5194/acp-11-6115-2011, 2011. 26913, 26916
Murphy, D. M. and Fahey, D. W.: An estimate of the flux of stratospheric reactive nitrogen and ozone into the troposphere, J. Geophys. Res., 99, 5325–5332, doi:10.1029/93JD03558, 1994. 26899
Myhre, G., Shine, K. P., Rädel, G., Gauss, M., Isaksen, I. S. A., Tang, Q., Prather, M. J., Williams, J. E., van Velthoven, P., Dessens, O., Koffi, B., Szopa, S., Hoor, P., Grewe, V., Borken-Kleefeld, J., Berntsen, T. K., and Fuglestvedt, J. S.: Radiative forcing due to changes in ozone and methane caused by the transport sector, Atmos. Environ., 45, 387–394, doi:10.1016/j.atmosenv.2010.10.001, 2011. 26898
Nassar, R., Logan, J. A., Worden, H. M., Megretskaia, I. A., Bowman, K. W., Osterman, G. B., Thompson, A. M., Tarasick, D. W., Austin, S., Claude, H., Dubey, M. K., Hocking, W. K., Johnson, B. J., Joseph, E., Merrill, J., Morris, G. A., Newchurch, M., Oltmans, S. J., Posny, F., Schmidlin, F. J., Vömel, H., Whiteman, D. N., and Witte, J. C.: Validation of Tropospheric Emission Spectrometer (TES) nadir ozone profiles using ozonesonde measurements, J. Geophys. Res., 113, D15S17, doi:10.1029/2007JD008819, 2008. 26914
Olsen, M. A., Schoeberl, M. R., and Douglass, A. R.: Stratosphere-troposphere exchange of mass and ozone, J. Geophys. Res., 109, D24114, doi:10.1029/2004JD005186, 2004. 26899
Olsen, M. A., Douglass, A. R., Newman, P. A., Gille, J. C., Nardi, B., Yudin, V. A., Kinnison, D. E., and Khosravi, R.: HIRDLS observations and simulation of a lower stratospheric intrusion of tropical air to high latitudes, Geophys. Res. Lett., 35, L21813, doi:10.1029/2008GL035514, 2008. 26912, 26916, 26941
Olsen, S. C., McLinden, C. A., and Prather, M. J.: Stratospheric N_2O–NO_y system: Testing uncertainties in a three-dimensional framework, J. Geophys. Res., 106, 28771–28784, 2001. 26899
OMI Team: Ozone Monitoring Instrument (OMI) Data User's Guide, OMI-DUG-3.0, http://disc.sci.gsfc.nasa.gov/Aura/additional/documentation/README.OMI_DUG.pdf, last access: 4 August 2010, 2009. 26903
Osterman, G., Bowman, K., Eldering, A., Fisher, B., Herman, R., Jacob, D., Jourdain, L.,

ACPD
11, 26897–26941, 2011

Kulawik, S., Luo, M., Monarrez, R., Paradise, S., Payne, V., Poosti, S., Richards, N., Rider, D., Shepard, D., Shephard, M., Vilnrotter, F., Worden, H., Worden, J., Yun, H., and Zhang, L.: Earth Observing System (EOS) Tropospheric Emission Spectrometer (TES) Level 2 (L2) Data User's Guide (Up to & including Version 4 data), Tech. Rep. D-38042, Version 4.0, JPL, Jet Propulsion Laboratory California Institute of Technology Pasadena, California, 91109-8099, 2009. 26903

Osterman, G. B., Kulawik, S. S., Worden, H. M., Richards, N. A. D., Fisher, B. M., Eldering, A., Shephard, M. W., Froidevaux, L., Labow, G., Luo, M., Herman, R. L., Bowman, K. W., and Thompson, A. M.: Validation of Tropospheric Emission Spectrometer (TES) measurements of the total, stratospheric, and tropospheric column abundance of ozone, J. Geophys. Res., 113, D15S16, doi:10.1029/2007JD008801, 2008. 26905

Pan, L. L., Randel, W. J., Gille, J. C., Hall, W. D., Nardi, B., Massie, S., Yudin, V., Khosravi, R., Konopka, P., and Tarasick, D.: Tropospheric intrusions associated with the secondary tropopause, J. Geophys. Res., 114, D10302, doi:10.1029/2008JD011374, 2009. 26911, 26912, 26916

Prather, M. J.: Numerical advection by conservation of second-order moments, J. Geophys. Res., 91, 6671–6681, 1986. 26901

Prather, M. J., Zhu, X., Tang, Q., Hsu, J., and Neu, J. L.: An atmospheric chemist in search of the tropopause, J. Geophys. Res., 116, D04306, doi:10.1029/2010JD014939, 2011. 26900, 26909

Richards, N. A. D., Osterman, G. B., Browell, E. V., Hair, J. W., Avery, M., and Li, Q.: Validation of Tropospheric Emission Spectrometer ozone profiles with aircraft observations during the Intercontinental Chemical Transport Experiment–B, J. Geophys. Res., 113, D16S29, doi:10.1029/2007JD008815, 2008. 26914

Roelofs, G. J. and Lelieveld, J.: Model study of the influence of cross-tropopause O_3 transports on tropospheric O_3 levels, Tellus B, 49, 38–55, 1997. 26898, 26899

Sander, S. P., Friedl, R. R., Golden, D. M., Kurylo, M. J., Moortgat, G. K., Keller-Rudek, H., Wine, P. H., Ravishankara, A. R., Kolb, C. E., Molina, M. J., Finlayson-Pitts, B. J., Huie, R. E., and Orkin, V. L.: Chemical Kinetics and Photochemical Data for Use in Atmospheric Studies, JPL Publication 06–2, NASA/JPL, Jet Propulsion Laboratory, California Institute of Technology, Pasadena, California, Evaluation Number 15, 2006. 26900

Schoeberl, M. R., Douglass, A. R., Hilsenrath, E., Bhartia, P. K., Beer, R., Waters, J. W., Gunson, M. R., Froidevaux, L., Gille, J. C., Barnett, J. J., Levelt, P. F., and DeCola, P.:

ACPD
11, 26897–26941, 2011

Overview of the EOS Aura Mission, IEEE Trans. Geosci. Remote Sens., 44, 1066–1074, doi:10.1109/TGRS.2005.861950, 2006. 26901, 26902

Shao, M., Lu, S., Liu, Y., Xie, X., Chang, C., Huang, S., and Chen, Z.: Volatile organic compounds measured in summer in Beijing and their role in ground-level ozone formation, J. Geophys. Res., 114, D00G06, doi:10.1029/2008JD010863, 2009. 26898

Tang, Q. and Prather, M. J.: Correlating tropospheric column ozone with tropopause folds: the Aura-OMI satellite data, Atmos. Chem. Phys., 10, 9681–9688, doi:10.5194/acp-10-9681-2010, 2010. 26900, 26901, 26903, 26907, 26910

Tang, Q., Prather, M. J., and Hsu, J.: Stratosphere-troposphere exchange ozone flux related to deep convection, Geophys. Res. Lett., 38, L03806, doi:10.1029/2010GL046039, 2011. 26900

Terao, Y., Logan, J. A., Douglass, A. R., and Stolarski, R. S.: Contribution of stratospheric ozone to the interannual variability of tropospheric ozone in the northern extratropics, J. Geophys. Res., 113, doi:10.1029/2008JD009854, 2008. 26898, 26899, 26906

Tiedtke, M.: A Comprehensive Mass Flux Scheme for Cumulus Parameterization in Large-Scale Models, Mon. Weather Rev., 117, 1779–1800, 1989. 26901

Waters, J. W., Froidevaux, L., Harwood, R. S., Jarnot, R. F., Pickett, H. M., Read, W. G., Siegel, P. H., Cofield, R. E., Filipiak, M. J., Flower, D. A., Holden, J. R., Lau, G. K., Livesey, N. J., Manney, G. L., Pumphrey, H. C., Santee, M. L., Wu, D. L., Cuddy, D. T., Lay, R. R., Loo, M. S., Perun, V. S., Schwartz, M. J., Stek, P. C., Thurstans, R. P., Boyles, M. A., Chandra, K. M., Chavez, M. C., Chen, G. S., Chudasama, B. V., Dodge, R., Fuller, R. A., Girard, M. A., Jiang, J. H., Jiang, Y., Knosp, B. W., LaBelle, R. C., Lam, J. C., Lee, K. A., Miller, D., Oswald, J. E., Patel, N. C., Pukala, D. M., Quintero, O., Scaff, D. M., Van Snyder, W., Tope, M. C., Wagner, P. A., and Walch, M. J.: The Earth Observing System Microwave Limb Sounder (EOS MLS) on the Aura Satellite, IEEE Trans. Geosci. Remote Sens., 44, 1075–1092, doi:10.1109/TGRS.2006.873771, 2006. 26902

Worden, H. M., Logan, J. A., Worden, J. R., Beer, R., Bowman, K., Clough, S. A., Eldering, A., Fisher, B. M., Gunson, M. R., Herman, R. L., Kulawik, S. S., Lampel, M. C., Luo, M., Megretskaia, I. A., Osterman, G. B., and Shephard, M. W.: Comparisons of Tropospheric Emission Spectrometer (TES) ozone profiles to ozonesondes: Methods and initial results, J. Geophys. Res., 112, D03309, doi:10.1029/2006JD007258, 2007. 26904

Zhang, L., Jacob, D. J., Liu, X., Logan, J. A., Chance, K., Eldering, A., and Bojkov, B. R.: Intercomparison methods for satellite measurements of atmospheric composition: appli-

ACPD

11, 26897–26941, 2011

cation to tropospheric ozone from TES and OMI, Atmos. Chem. Phys., 10, 4725–4739, doi:10.5194/acp-10-4725-2010, 2010. 26907, 26914

ACPD
11, 26897–26941, 2011

Table 1. Means and RMS of the exact matching TES and CTM partial ozone columns (unit: DU) of the TES swath shown in Fig. 4i covering 31.5° S–71.4° N with 54 individual profiles[a].

Regions	CTM ($\pm\sigma$)	CTM*	TES	CTM′ – TES′	CTM*′ – TES′
Upper Trop. (400 hPa–TPP)	13.1 (±3.1)	16.1	14.1	3.3	3.4
Mid Trop. (700–400 hPa)	12.8 (±2.0)	12.1	11.1	1.9	1.7
Lower Trop. (surf.–700 hPa)	12.1 (±3.1)	9.9	9.3	2.0	1.6

[a] Single values are the means, while the differences are the RMS of anomalies (e.g., $\mathrm{CTM}' = \mathrm{CTM} - \overline{\mathrm{CTM}}$). CTM* represents the CTM values processed with the TES operator.

ACPD
11, 26897–26941, 2011

Table 2. Mean biases and RMS errors (unit: ppb) of CTM versus MLS, HIRDLS, and TES for five regions at 215 hPa and 147 hPa for July 2005[a].

	MLS		HIRDLS		TES		TES*	
Regions	215 hPa	147 hPa	215 hPa	147 hPa	215 hPa	147 hPa	215 hPa	147 hPa
NH Mid-L	10.0±79.2	51.6±125.6	−48.1±186.7	34.8±144.1	7.9±42.1	23.7±75.8	−22.2±79.8	−5.1±154.0
NH Jet	7.0±57.0	11.7±135.6	−15.1±60.9	−32.6±157.5	5.1±25.0	11.1±53.8	−2.8±34.1	−5.3±105.9
Tropics	8.6±45.3	−12.2±151.8	−6.6±34.5	−63.3±183.2	11.7±17.7	21.0±41.3	2.5±17.8	−5.3±85.6
SH Jet	42.3±80.0	150.7±162.1	58.4±109.6	136.0±174.9	72.6±69.7	129.6±113.7	34.8±84.1	133.6±159.3
SH Mid-L	43.7±106.8	386.9±301.7	96.2±229.7	393.3±343.8	77.5±71.8	225.1±196.5	90.8±131.9	328.1±294.2

[a]The latitude ranges are NH middle latitude (40° N–50° N), NH jet (25° N–35° N), tropics (15° S–15° N), SH jet (35° S–25° S), and SH middle latitude (50° S–40° S). The results are shown in the format of the mean bias±RMS and defined as the CTM less Aura. The observation times (N) is shown in Figs. 5 and 6 and the SEM values are generally about 1 ppb and less than 3 ppb. TES* denotes the comparisons with the raw CTM outputs.

ACPD
11, 26897–26941, 2011

Table 3. Same as Table 2 for January 2006[a].

	MLS		HIRDLS		TES		TES*	
Regions	215 hPa	147 hPa	215 hPa	147 hPa	215 hPa	147 hPa	215 hPa	147 hPa
NH Mid-L	61.4±121.2	344.1±257.7	105.9±823.9	344.8±288.2	73.9±67.3	155.3±111.4	94.4±129.9	331.6±297.7
NH Jet	37.0±77.0	61.4±209.8	52.3±94.4	56.0±174.6	30.7±39.6	44.6±94.6	33.8±86.1	53.1±180.3
Tropics	11.0±66.4	−13.2±242.5	5.2±74.4	−26.2±212.3	8.4±40.4	14.7±107.0	7.1±68.2	1.5±167.4
SH Jet	5.8±70.9	37.3±201.0	11.8±76.9	13.0±187.0	22.6±33.9	61.7±76.4	1.0±81.9	5.1±178.9
SH Mid-L	49.4±79.3	188.4±150.6	87.9±138.7	210.7±165.4	54.7±45.9	148.9±106.0	37.9±96.9	92.7±155.6

[a]The observation times (N) is shown in Figs. 7 and 8.

ACPD
11, 26897–26941, 2011

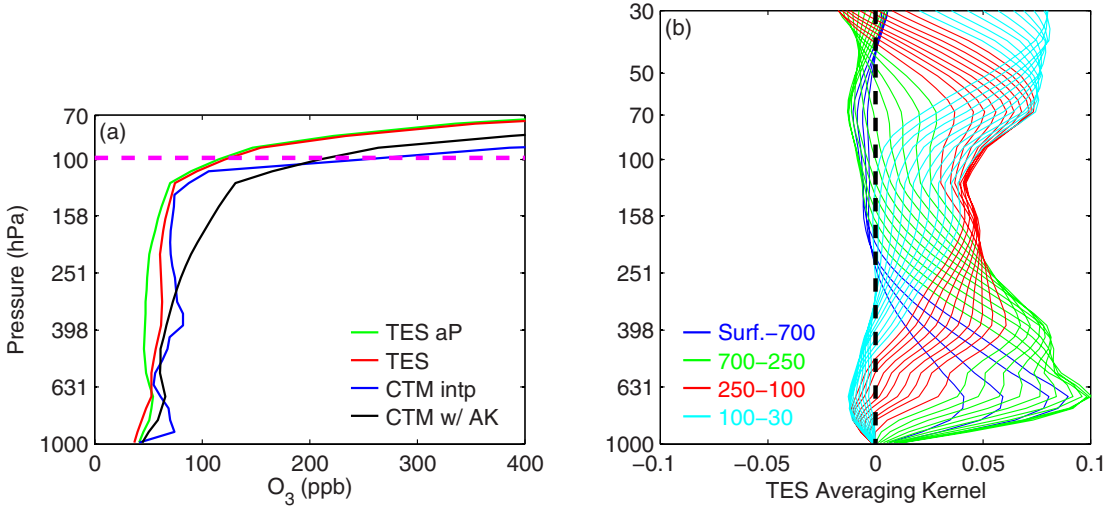

Fig. 1. Comparisons between TES a priori (green), TES (red), linearly interpolated CTM on TES levels (blue) and convolved CTM (black) ozone profiles (**a**, unit: ppb) and the corresponding TES averaging kernel (AK, **b**) as a function of pressure at 9.5° S, 295.0° E on 25 August 2005. On the left panel, dashed magenta line shows the e90 tropopause of 99 hPa. The AK for different pressure ranges are represented by solid lines: blue for surface–700 hPa, green for 700–250 hPa, red for 250–100 hPa, and cyan for 100–30 hPa. The dashed black line shows the zero line. The DOFS for the troposphere and the whole atmosphere are 1.5 and 4.0, respectively.

ACPD
11, 26897–26941, 2011

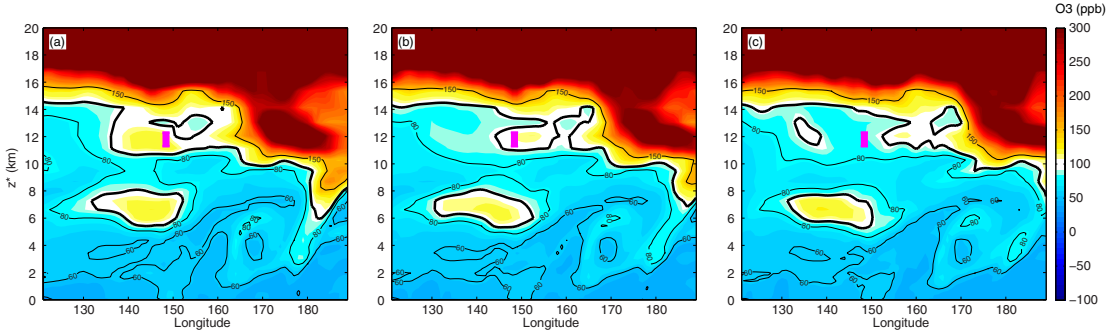

Fig. 2. Pressure altitude (z^*) by longitude (120–190° E) plots of simulated ozone (colors: blue show low values, red high values, unit: ppb) at 29.5° N on 31 January 2005 **(a)** 00:00 UTC, **(b)** 02:00 UTC, and **(c)** 04:00 UTC. The thin black contour lines represent ozone of 60, 80, and 150 ppb. The thick black contour lines define the 100-ppb ozone surface (approximately the tropopause). The magenta squares correspond to the same CTM grid box.

ACPD
11, 26897–26941, 2011

Aura measurements and cross-tropopause ozone flux

Q. Tang and M. J. Prather

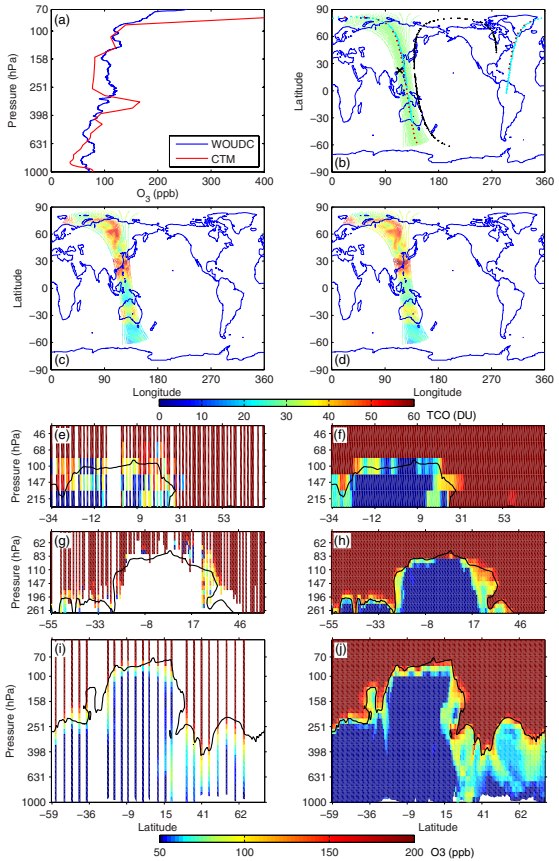

Fig. 3. Comparisons between sonde and Aura ozone swaths with CTM for 23 March 2005. **(a)** WOUDC sonde (blue, 05:26 UTC) vs. CTM (red, 06:00 UTC) profile (unit: ppb) at Hong Kong (22.3° N, 114.2° E, station code 344). **(b)** The locations of available Aura measurements (on the CTM grid) during 05:00–06:00 UTC. HIRDLS: black crosses, MLS: cyan crosses, TES: red crosses, OMI: green dots, sonde location in **(a)**: the large black cross. Comparisons for Aura (left) vs. exact matching CTM results (right) swaths: **(c)** vs. **(d)** for OMI; **(e)** vs. **(f)** for MLS; **(g)** vs. **(h)** for HIRDLS; **(i)** vs. **(j)** for TES. We compare latitude-by-longitude TCO (unit: DU) for OMI swaths, altitude-by-latitude O_3 molar ratios (0–180° E, unit: ppb) for HIRDLS, MLS, and TES. The black lines in **(e)**–**(j)** represent the e90 tropopause.

ACPD
11, 26897–26941, 2011

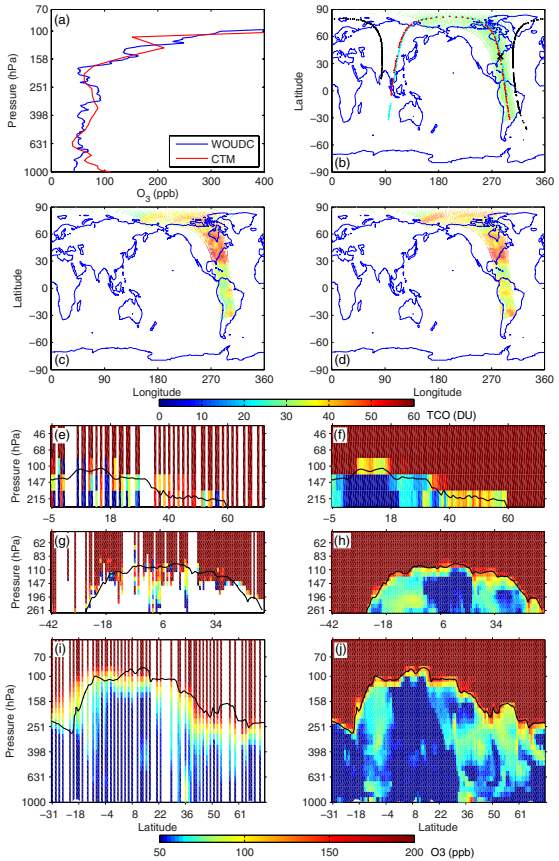

Fig. 4. Same as Fig. 3 for 25 August 2005. The sonde is from Wallops Island (37.9° N, 75.5° W, station code 107) at 17:39 UTC, compared with model simulation at 18:00 UTC in **(a)**. The Aura and CTM swaths are for 18:00–19:00 UTC. **(c)**–**(j)** show the swaths in 180–360° E.

ACPD
11, 26897–26941, 2011

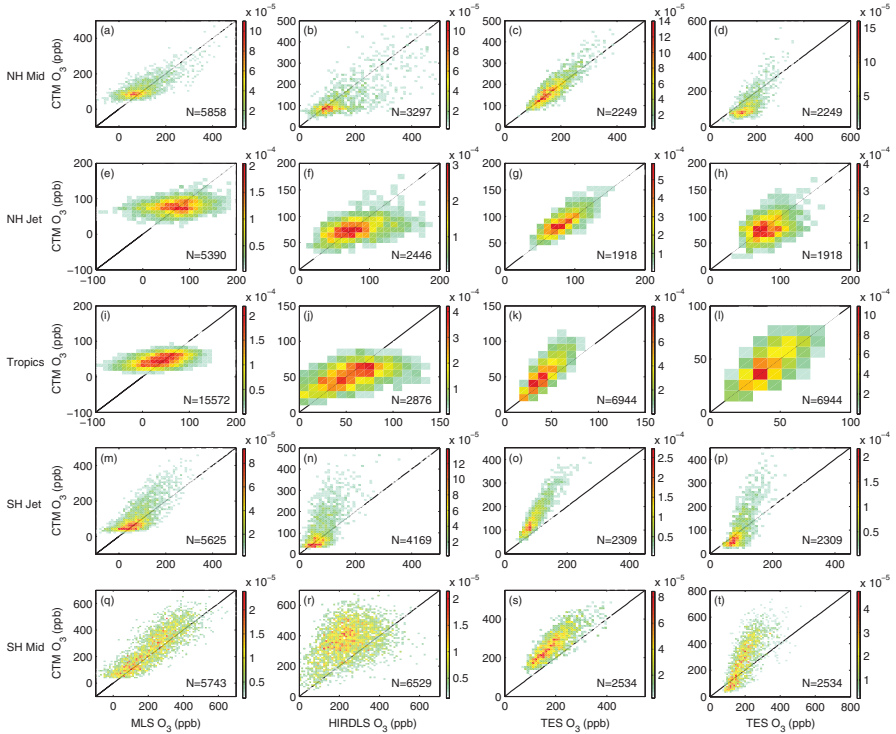

Fig. 5. 2-D probability density functions (PDFs, unit: ppb^{-2}) of CTM vs. Aura O_3 for July 2005 at 215 hPa. Rows from top to bottom are for NH middle latitudes (40° N–50° N), NH jet (25° N–35° N), tropics (15° S–15° N), SH jet (35° S–25° S), and SH middle latitudes (50° S–40° S). Comparisons for different Aura ozone datasets are presented in columns from left to right: MLS, HIRDLS, and TES. The CTM results processed with the TES operator are shown in the third column, with the raw model results in the fourth column. The 2-D PDF includes all the good CTM-Aura pairs in the month and is weighted by the inverse of observation times for each latitude. It is normalized to give a 2-D integral of 1. N is the number of comparisons and the solid black line shows the 1:1 line. The mean biases and RMS are given in Table 2.

ACPD
11, 26897–26941, 2011

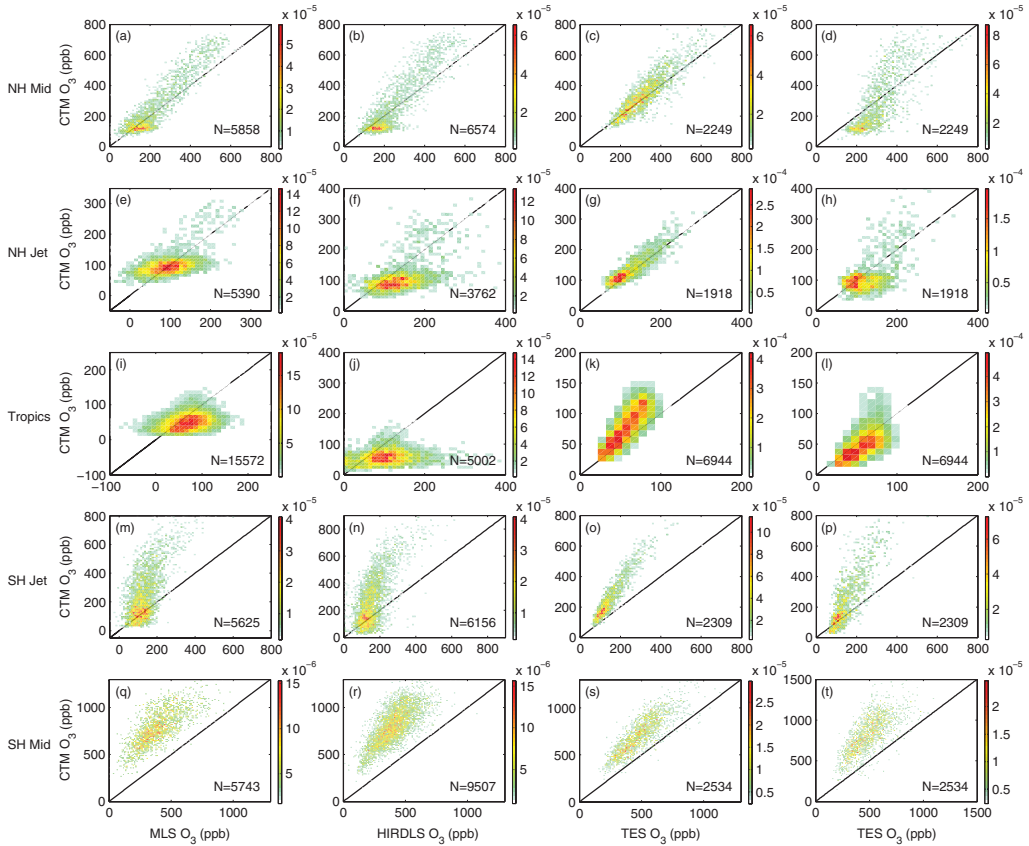

Fig. 6. Same as Fig. 5 for July 2005 at 147 hPa.

ACPD
11, 26897–26941, 2011

Aura measurements and cross-tropopause ozone flux

Q. Tang and M. J. Prather

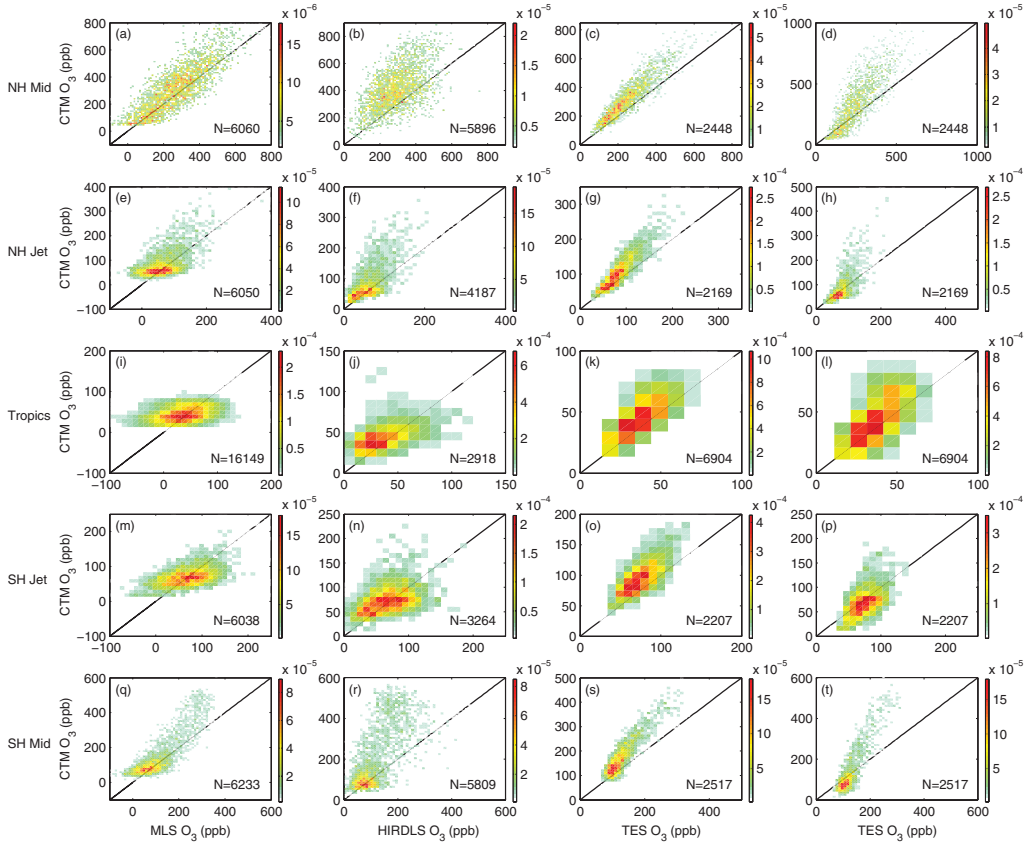

Fig. 7. Same as Fig. 5 for January 2006 at 215 hPa. The mean biases and RMS are given in Table 3.

ACPD
11, 26897–26941, 2011

Aura measurements and cross-tropopause ozone flux

Q. Tang and M. J. Prather

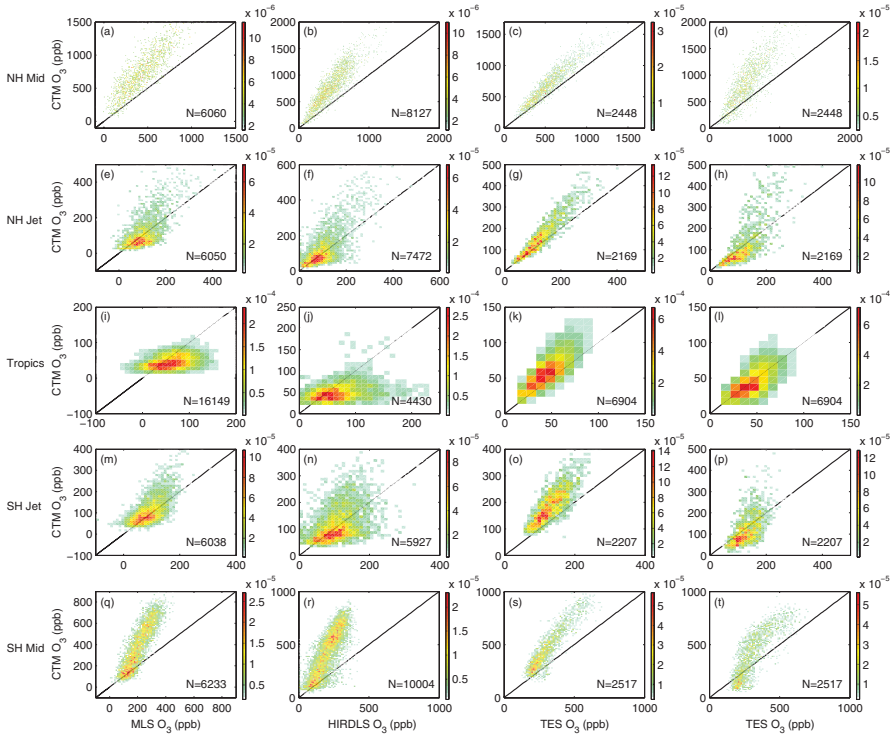

Fig. 8. Same as Fig. 5 for January 2006 at 147 hPa. The mean biases and RMS are given in Table 3.

ACPD
11, 26897–26941, 2011

Aura measurements and cross-tropopause ozone flux

Q. Tang and M. J. Prather

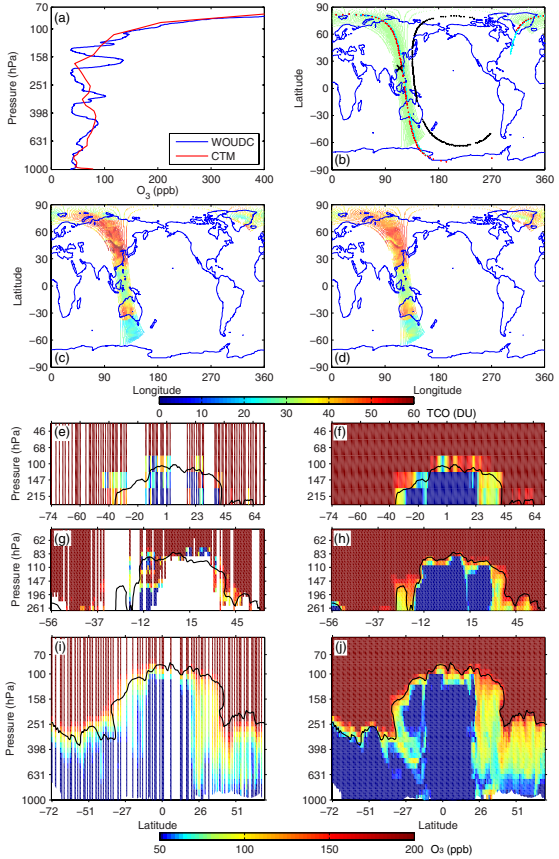

Fig. A1. Same as Fig. 3 for 27 July 2005. The sonde was measured at 05:22 UTC, compared with model simulation at 06:00 UTC in **(a)**. The Aura and CTM swaths are for 05:00–06:00 UTC. **(c)**–**(j)** show the swaths in 0–180° E.

ACPD
11, 26897–26941, 2011

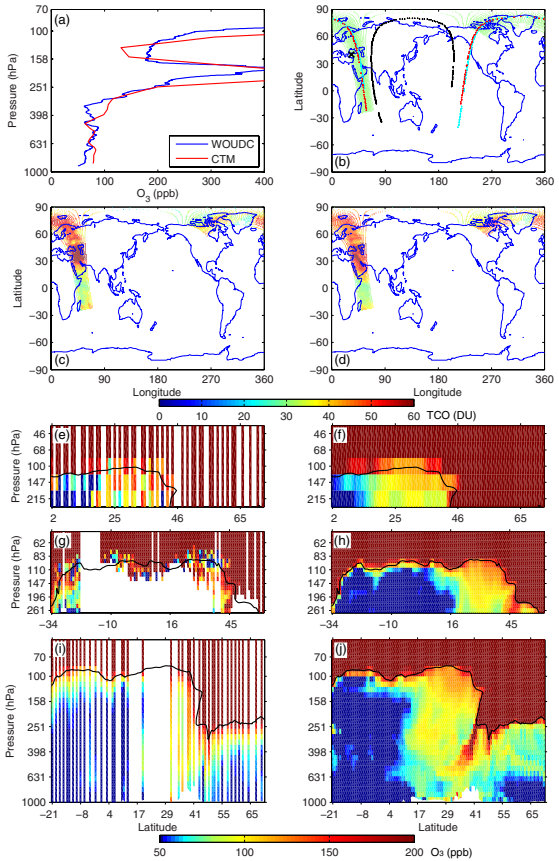

Fig. A2. Same as Fig. 3 for 6 July 2005. The sonde is from Ankara (40.0° N, 32.9° E, station code 348) at 11:52 UTC, compared with model simulation at 12:00 UTC in **(a)**. The Aura and CTM swaths are for 10:00–11:00 UTC. **(c)**–**(j)** show the swaths in 0–134° E.

ACPD
11, 26897–26941, 2011

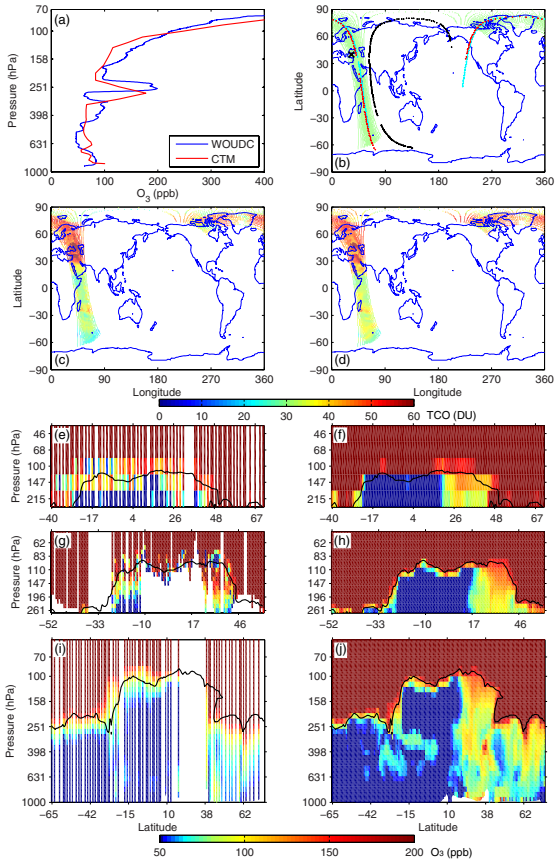

Fig. A3. Same as Fig. 2 for 20 July 2005. The sonde was measured at 11:37 UTC, compared with model simulation at 12:00 UTC in **(a)**. The Aura and CTM swaths are for 10:00–11:00 UTC. **(c)**–**(j)** show the swaths in 0–99° E.

ACPD
11, 26897–26941, 2011

Aura measurements and cross-tropopause ozone flux

Q. Tang and M. J. Prather

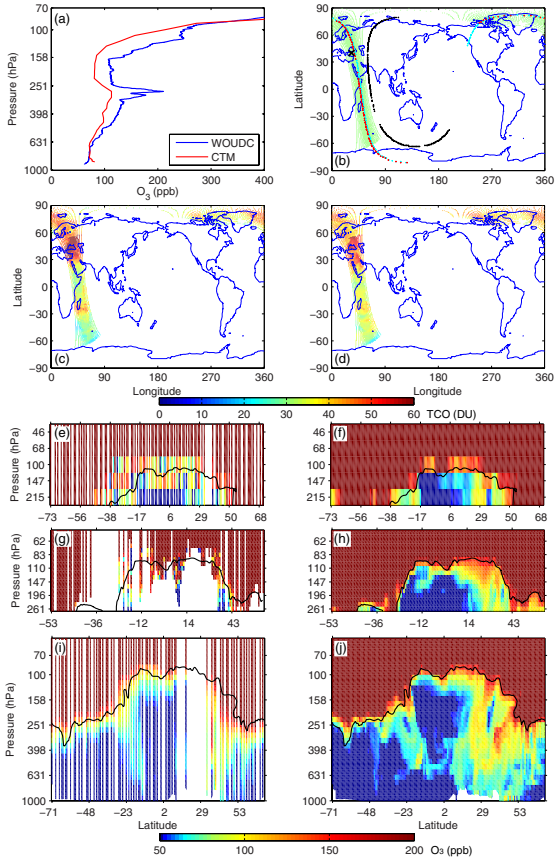

Fig. A4. Same as Fig. 2 for 3 August 2005. The sonde was measured at 11:36 UTC.

ACPD
11, 26897–26941, 2011

Aura measurements and cross-tropopause ozone flux

Q. Tang and M. J. Prather

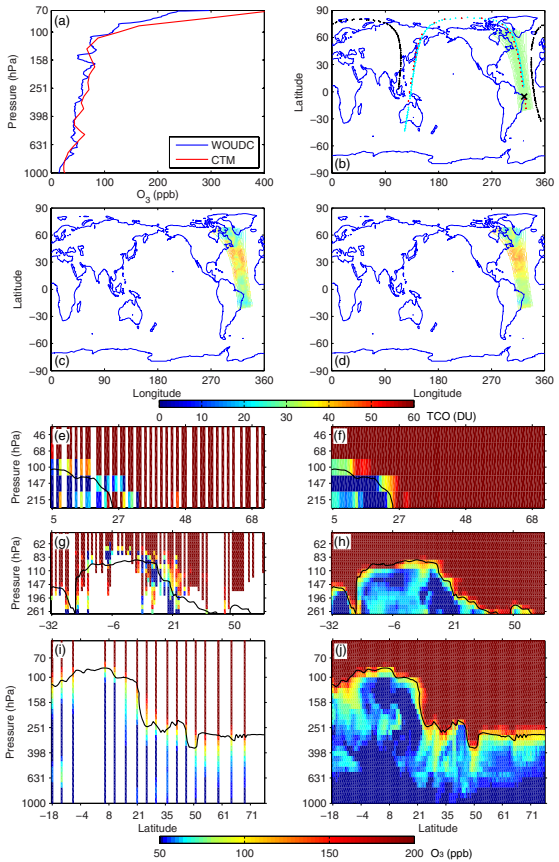

Fig. A5. Same as Fig. 3 for 2 February 2005. The sonde is from Maxaranguape (5.4° S, 35.4° W, station code 466) at 15:45 UTC, compared with model simulation at 16:00 UTC in **(a)**. The Aura and CTM swaths are for 16:00–17:00 UTC. **(c)**–**(j)** show the swaths in 251–360° E.

ACPD
11, 26897–26941, 2011

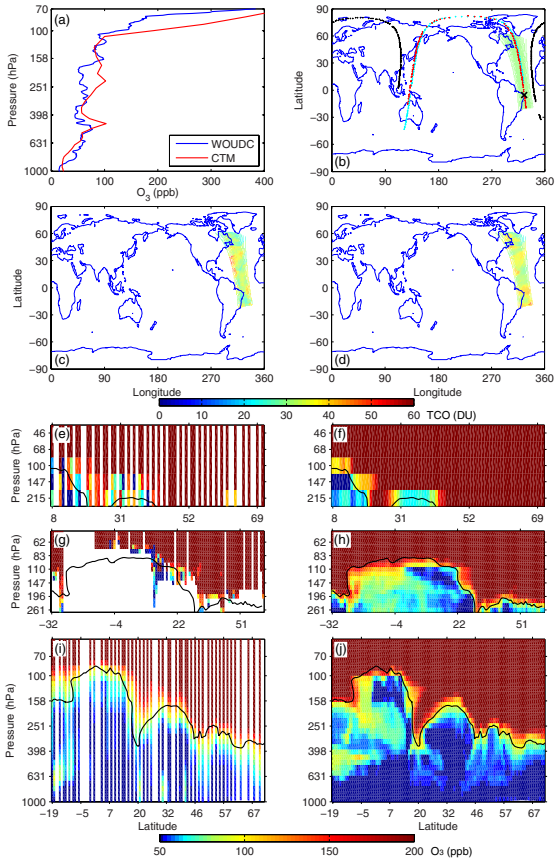

Fig. A6. Same as Fig. 5 for 19 December 2005. The sonde was measured at 16:00 UTC.

ACPD
11, 26897–26941, 2011

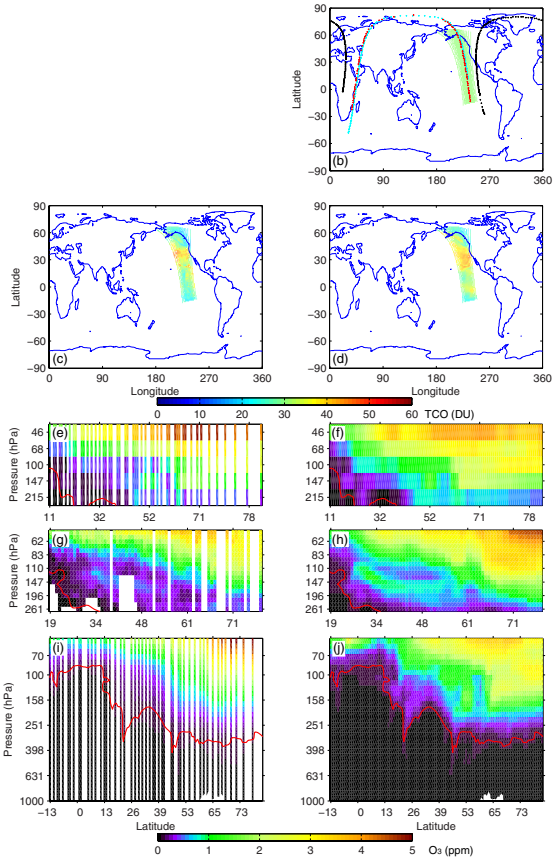

Fig. A7. Same as Fig. 3 for 26 January 2006 except that no sonde is available and the e90 tropopause is indicated by red solid lines in **(e)**–**(j)**. The Aura and CTM swaths are for 22:00–23:00 UTC. **(c)**–**(j)** show the swaths in 181–270° E. **(g)** and **(h)** only show the HIRDLS swath at 19–74° N to mimic the Fig. 1 of Olsen et al. (2008).

ACPD
11, 26897–26941, 2011